AIAA JOURNAL
Vol. 34, No. 7, July 1996

Computation of Unsteady Three-Dimensional Transonic Nozzle Flows Using k–ε Turbulence Closure

G. A. Gerolymos* and I. Vallet†
Université Pierre-et-Marie-Curie, 91405 Orsay, Paris, France
and
A. Bölcs‡ and P. Ott§
Ecole Polytechnique Fédérale de Lausanne, Lausanne CH-1015, Switzerland

A three-dimensional Navier–Stokes solver is applied to the computation of unsteady nozzle flows resulting from fluctuating backpressure and validated by comparison with experimental measurements. The flow is modeled by the three-dimensional compressible Navier–Stokes equations using the Launder–Sharma near-wall k–ε turbulence model. The mean-flow and turbulence-transport equations are integrated in time using a first-order implicit scheme with third-order MUSCL upwind-biased Van Leer flux-vector-splitting. The configuration studied is a three-dimensional nozzle, with thick sidewall boundary layers. The three-dimensional effect is produced by the shock wave–boundary layer interaction at the corners of the nozzle, where an important three-dimensional recirculating zone appears. The flow is unsteady because of backpressure fluctuation, produced experimentally by a rotating rod of elliptical cross section. The unsteady computations were run for a backpressure fluctuation frequency of 180 Hz. The computed and measured results compare satisfactorily. An analysis of steady and unsteady losses is undertaken.

Introduction

THE computation of unsteady separated flows is a major field of computational fluid dynamics development. Many workers recognize the advantage of using transport-equation models of turbulence, which, as remarked by Ekaterinaris and Menter,[1] avoid the "ambiguity that comes from the difficulty of defining length-scales" necessary for algebraic turbulence models. Recent work in the field has been reported by Rizzetta and Visbal,[2] who computed subsonic dynamic stall over an airfoil using the two-dimensional compressible Navier–Stokes equations with near-wall k–ϵ turbulence closure. Ekaterinaris and Menter[1] computed two-dimensional compressible separated flow around an oscillating airfoil using near-wall k–ϵ and k–ω turbulence closures. Jin and Braza[3] have studied the large structures of separated two-dimensional incompressible high-incidence flow around an airfoil using a modified k–ε subgrid turbulence closure. Shih et al.[4] have computed the two-dimensional unsteady supersonic flow over a cavity, using a modified near-wall k–ε turbulence closure. The same configuration has been studied three-dimensionally by Rizzetta[5] who used an algebraic turbulence model.

The validity of existing two-equation turbulence closures for unsteady flows has been investigated by Fan et al.,[6] who concluded that the use of $n^+ = n u_\tau \breve{\nu}_w^{-1}$ (where n is the distance from the wall, u_τ is the friction velocity, and $\breve{\nu}_w$ is the kinematic viscosity at the wall) in the near-wall damping terms is a dubious choice, at least as far as unsteady flows are concerned. This brings forward k–ε models that use only the turbulence-Reynolds-number $Re_T = k^2 \breve{\nu}^{-1} \varepsilon^{*-1}$ (where k is the turbulence kinetic energy, $\breve{\nu}$ is the kinematic viscosity, and ε^* is the isotropic part of the dissipation), such as the Launder–Sharma[7] closure. A new model was developed by Fan et al.[6] that uses a combination of Re_T and a distance-from-the-wall Reynolds number, where the velocity scale is based on the turbulence kinetic energy ($Re_n = n\sqrt{k}\, \breve{\nu}^{-1}$).

For aeroelastic stability computations, both for aircraft[8–11] and for turbomachinery[12,13] applications, the frequency of the unsteady flow is relatively low with respect to the characteristic frequency of turbulence, their ratio being characterized by the nondimensional near-wall similarity parameter l_s^+ (Ref. 6), or inner-variables-scaled nondimensional frequency f^+ (Ref. 14), defined by

$$l_s^+ = \sqrt{u_\tau^2 / \pi f \breve{\nu}} = \sqrt{1/\pi f^+}, \qquad f^+ = f\breve{\nu}/u_\tau^2 \tag{1}$$

In most aeroelastic problems, l_s^+ is sufficiently high (f^+ is sufficiently low) that the modulation of turbulence by the driving unsteady phenomenon is negligible.[15] In these cases, it is plausible to expect adequate results from classic models such as the Launder–Sharma k–ε closure. The tensor-invariant form of the near-wall terms is very attractive because it is independent of the distance from the wall and of the wall orientation, an advantage recognized by several authors.[16–19]

The unsteady flow in a Laval nozzle caused by fluctuating backpressure has been studied by various authors, using Euler equations.[20–24] As early as 1984, Liou and Coakley[25] investigated the unsteady two-dimensional transonic flow in diffusers using the two-dimensional Navier–Stokes equations with k–ω^2 turbulence closure, using grids where the first grid point away from the wall was at $n_w^+ \cong 5$. Both forced and natural flow oscillations were studied.

The previous literature overview indicates that the validity of two-equation closures for unsteady internal transonic flows has only been tested two-dimensionally. Careful investigation of existing experimental data for transonic shock wave–boundary layer interaction[26] suggests that there invariably exists nonnegligible three-dimensional contamination of nominally two-dimensional configurations. Therefore, assessing the validity and drawbacks of models is only possible by three-dimensional computations. With this objective, the unsteady three-dimensional transonic flow in a Laval nozzle, caused by fluctuating backpressure, using the Navier–Stokes equations with the Launder–Sharma[7] near-wall turbulence closure, is studied in this work. The numerical method is based on the steady flow solver developed by Gerolymos and Vallet.[26] The configuration studied has been investigated experimentally by Ott et al.[23] The numerical computations are compared with measurements. An analysis attempting to quantify steady and unsteady losses is attempted.

Received Aug. 28, 1995; revision received Feb. 23, 1996; accepted for publication March 11, 1996.

*Professor, Director, Laboratoire d'Energétique, Unité de Recherche Associée au Centre National de Recherche Scientifique 1504, Building 511.

†Ministry of Scientific Research Research Assistant, Unité de Recherche Associée au Centre National de Recherche Scientifique 1504, Building 511.

‡Professor, Director, Laboratoire de Thermique Appliquée et de Turbomachines.

§Research Engineer, Laboratoire de Thermique Appliquée et de Turbomachines-Département de Génie Mécanique.

Flow Model and Computational Method

Flow Model

The flow is modeled by the compressible Favre–Reynolds-averaged three-dimensional Navier–Stokes equations, with the Launder–Sharma[7] near-wall k–ε closure, written in tensor-invariant form[16–19]:

$$\frac{\partial\bar{\rho}}{\partial t}+\operatorname{div}(\bar{\rho}\tilde{\boldsymbol{V}})=0$$

$$\frac{\partial\bar{\rho}\tilde{\boldsymbol{V}}}{\partial t}+\operatorname{div}[\bar{\rho}\tilde{\boldsymbol{V}}\otimes\tilde{\boldsymbol{V}}-\bar{\boldsymbol{\tau}}+\bar{\rho}\widetilde{\boldsymbol{V}''\otimes\boldsymbol{V}''}]=0$$

$$\frac{\partial(\bar{\rho}\breve{h}_t-\bar{p})}{\partial t}+\operatorname{div}[\bar{\rho}\tilde{\boldsymbol{V}}\breve{h}_t-\tilde{\boldsymbol{V}}\cdot(\bar{\boldsymbol{\tau}}-\bar{\rho}\widetilde{\boldsymbol{V}''\otimes\boldsymbol{V}''})$$

$$+\,(\bar{\boldsymbol{q}}+\bar{\rho}\widetilde{e''\boldsymbol{V}''})]=-\left[P_k-\bar{\rho}\varepsilon^*-2\breve{\mu}(\operatorname{grad}\sqrt{k})^2\right] \tag{2}$$

$$\frac{\partial\bar{\rho}k}{\partial t}+\operatorname{div}\left[\bar{\rho}\tilde{\boldsymbol{V}}k-\left(\breve{\mu}+\frac{\mu_T}{\sigma_k}\right)\operatorname{grad}k\right]$$

$$=\left[P_k-\bar{\rho}\varepsilon^*-2\breve{\mu}(\operatorname{grad}\sqrt{k})^2\right]$$

$$\frac{\partial\bar{\rho}\varepsilon^*}{\partial t}+\operatorname{div}\left[\bar{\rho}\tilde{\boldsymbol{V}}\varepsilon^*-\left(\breve{\mu}+\frac{\mu_T}{\sigma_\varepsilon}\right)\operatorname{grad}\varepsilon^*\right]$$

$$=\left[C_{\varepsilon1}P_k\frac{\varepsilon^*}{k}-C_{\varepsilon2}f_{\varepsilon2}\bar{\rho}\frac{\varepsilon^{*2}}{k}+2\frac{\breve{\mu}\mu_T}{\bar{\rho}}(\nabla^2\tilde{\boldsymbol{V}})^2\right]$$

$$\bar{p}=\bar{\rho}R_g\tilde{T}=\bar{\rho}[(\gamma-1)/\gamma]\tilde{h}=\bar{\rho}(\gamma-1)\tilde{e}$$

$$-\bar{\rho}\widetilde{\boldsymbol{V}''\otimes\boldsymbol{V}''}\cong2\mu_T\left[\breve{\boldsymbol{D}}-\tfrac{2}{3}\operatorname{div}\tilde{\boldsymbol{V}}\boldsymbol{I}\right]-\tfrac{2}{3}\bar{\rho}k\boldsymbol{I} \tag{3}$$

$$\bar{\rho}\widetilde{e''\boldsymbol{V}''}\cong-\kappa_T\operatorname{grad}\tilde{T}$$

where t is the time; $\tilde{\boldsymbol{V}}$ is the velocity; $\bar{\rho}$ is the density; $\bar{p}$ is the pressure; $\tilde{T}$ is the temperature; $\tilde{h}$ is the enthalpy; $\gamma=1.4$ is the isentropic exponent; $R_g=287.04\,\mathrm{m^2\,s^{-2}\,K^{-1}}$ is the gas-constant for air; $\breve{h}_t=\tilde{h}+\frac{1}{2}\tilde{V}^2$ is the total enthalpy of the mean flow[27] (which is different from $\tilde{h}_t=\breve{h}_t+k$); k is the turbulence kinetic energy; ε^* is the isotropic part of the turbulence-kinetic-energy dissipation rate $[\bar{\rho}\varepsilon^*=\bar{\rho}\varepsilon-2\breve{\mu}\,(\operatorname{grad}\sqrt{k})^2$, where ε is the dissipation-rate]; $P_k=-\bar{\rho}\widetilde{\boldsymbol{V}''\otimes\boldsymbol{V}''}$; $\breve{\boldsymbol{D}}$ is the turbulence-kinetic-energy production; $\bar{\boldsymbol{\tau}}$ is the viscous stress tensor, $\bar{\boldsymbol{q}}\cong-\breve{\kappa}\operatorname{grad}\tilde{T}$ is the heat-flux-vector, $\breve{\boldsymbol{D}}=\frac{1}{2}[\operatorname{grad}\tilde{\boldsymbol{V}}+(\operatorname{grad}\tilde{\boldsymbol{V}})^T]$ is the rate-of-deformation tensor; $\boldsymbol{I}$ is the identity tensor; $\breve{\mu}=\mu(\tilde{T})$ is the molecular dynamic viscosity at temperature $\tilde{T}$; μ_T is the eddy viscosity; $\breve{\kappa}=\kappa(\tilde{T})$ is the molecular heat conductivity at temperature $\tilde{T}$; κ_T is the eddy heat conductivity; $(\tilde{\cdot})$ denotes Favre-averaging [with fluctuations $('')$]; $(\bar{\cdot})$ denotes nonweighted-averaging [with fluctuations $(\cdot')$]; and $(\breve{\cdot})$ denotes functions of mean flow quantities that cannot be identified with the preceding averages. The model constants, model functions, molecular diffusion coefficients and other details are given by Gerolymos and Vallet.[26]

Numerics and Boundary Conditions

The mean-flow and turbulence-transport equations are discretized in space, on a structured grid, using a third-order upwind-biased MUSCL scheme with Van Leer flux-vector splitting and Van Albada limiters. The resulting semidiscrete scheme is integrated in time using a first-order implicit procedure. The mean-flow and turbulence-transport equations are integrated simultaneously. The Jacobian-flux matrix is computed using a first-order space discretization, to reduce bandwidth, and factored. The resulting linear systems are solved by LU decomposition. The numerical method is described in detail by Gerolymos and Vallet.[26]

The time step is based on a combined convective (Courant) and viscous (von Neumann) criterion[26]:

$$\Delta t=\mathrm{CFL}_{\max}\min_{i,j,k}\left[\frac{l_g}{\tilde{V}+\breve{a}\sqrt{1+\frac{5}{6}(\gamma-1)M_T^2}},\ \frac{l_g^2}{2\nu_{\mathrm{eq}}}\right] \tag{4}$$

where l_g is the grid-cell size, $\tilde{V}$ is the flow velocity, $\breve{a}$ is the sound velocity, $M_T=\sqrt{(2k\breve{a}^{-2})}$ is the turbulence Mach number, and ν_{eq} is the equivalent diffusivity, computed by MacCormack.[26,28] For the unsteady computations presented in this work, the maximum Courant–Friedrichs–Lewy ($\mathrm{CFL}_{\max}$) $\cong$ 500.

In this work one-fourth of the nozzle was discretized. At the upstream boundary, a reservoir condition was applied (because the flow is choked and no perturbation reaches the upstream boundary). This condition as well as the no-slip wall boundary-condition and the symmetry conditions at the symmetry plane are identical with those used in the steady-flow computations described by Gerolymos and Vallet.[26] At the outflow boundary, the pressure signal is imposed, described as the sum of 12 time harmonics obtained from the measurements:

$$\bar{p}_2(t)={}^0\bar{p}_2+\sum_{m=1}^{12}\left[|{}^m\hat{\bar{p}}_2|\cos(2\pi mft+{}^m\varphi_2)\right]$$

$$\Rightarrow\frac{\partial\bar{p}_2}{\partial t}=-\sum_{m=1}^{12}\left[2\pi mf|{}^m\hat{\bar{p}}_2|\sin(2\pi mft+{}^m\varphi_2)\right] \tag{5}$$

where ${}^0\bar{p}_2$, is the time-mean outflow pressure, $|{}^m\hat{\bar{p}}_2|$ and ${}^m\varphi_2$ are the amplitudes and phase angles of the Fourier coefficients, and m is the harmonic number. Because experimental measurements were available only at the wall, it was assumed that pressure is homogeneous on the exit plane. The outflow boundary-condition imposes the pressure (and its time derivative in the implicit phase of the scheme) and extrapolates all other variables ($\bar{\rho}$, $\tilde{\boldsymbol{V}}$, k, ε^*).[26] To achieve high time steps, it is indispensible to apply boundary conditions both implicitly and explicitly.

Experimental Setup

The experimental setup has been described in detail by Ott et al.,[23] and only a brief overview is given here. A Laval nozzle with a width of 40 mm was equipped with nozzle liners, giving a converging–diverging section (Fig. 1). The inlet and outlet height of the test section is 80 mm, and the throat height is 71 mm. A continuously running four-stage radial turbocompressor was used as the air source.

On the nozzle liners, the boundary layer was cut off before the throat (Fig. 1). On the sidewalls, the boundary layers were not modified. These relatively thick sidewall boundary layers interact with the shock wave at the nozzle corners and produce the significant three-dimensional effects observed. At the exit section of the nozzle, a cylindrical rod with elliptical cross section (3 × 5 mm) is rotated by a hydraulic motor. The rod is situated 480 mm downstream of the throat. The blockage and wake losses of the rod induce a shock wave in the test section, which oscillates with the rotation of the rod. The rotation frequency of the rod can be varied in the range 0–180 Hz.

Steady-state pressure taps are mounted on the nozzle liners and on the sidewall, at the symmetry planes of the nozzle (Fig. 1). Unsteady pressures are measured using eight unsteady pressure transducers[23] mounted on the sidewall y-symmetry plane (one transducer located 164 mm downstream of the throat and seven transducers spaced 5 mm apart in the shock-wave neighborhood) (Fig. 1). The downstream unsteady transducer records the unsteady pressure signal that is applied as a downstream boundary condition for the computations [Eq. (5)]. Optical instrumentation was also available and was used to study the oscillatory motion of the shock wave.[23]

Steady Computations

Ott et al.[23] presented two-dimensional Euler computations (where the time-average backpressure was adjusted to get the correct shock-wave position) that accurately predicted the shock-wave oscillatory displacement at the y-symmetry plane (the system of coordinates is shown in Fig. 1). Gerolymos and Bréus[24] repeated these computations using rather fine grids for an Euler code (264 × 41) and obtained analogous results. Preliminary two-dimensional steady Navier-Stokes computations (at the z-symmetry plane) using the Launder–Sharma k–ε closure[7] gave unsatisfactory results for the pressure distribution, suggesting that, because of the small width of the nozzle and of the rather thick sidewall boundary layers, three-dimensional effects are important for this configuration (optical

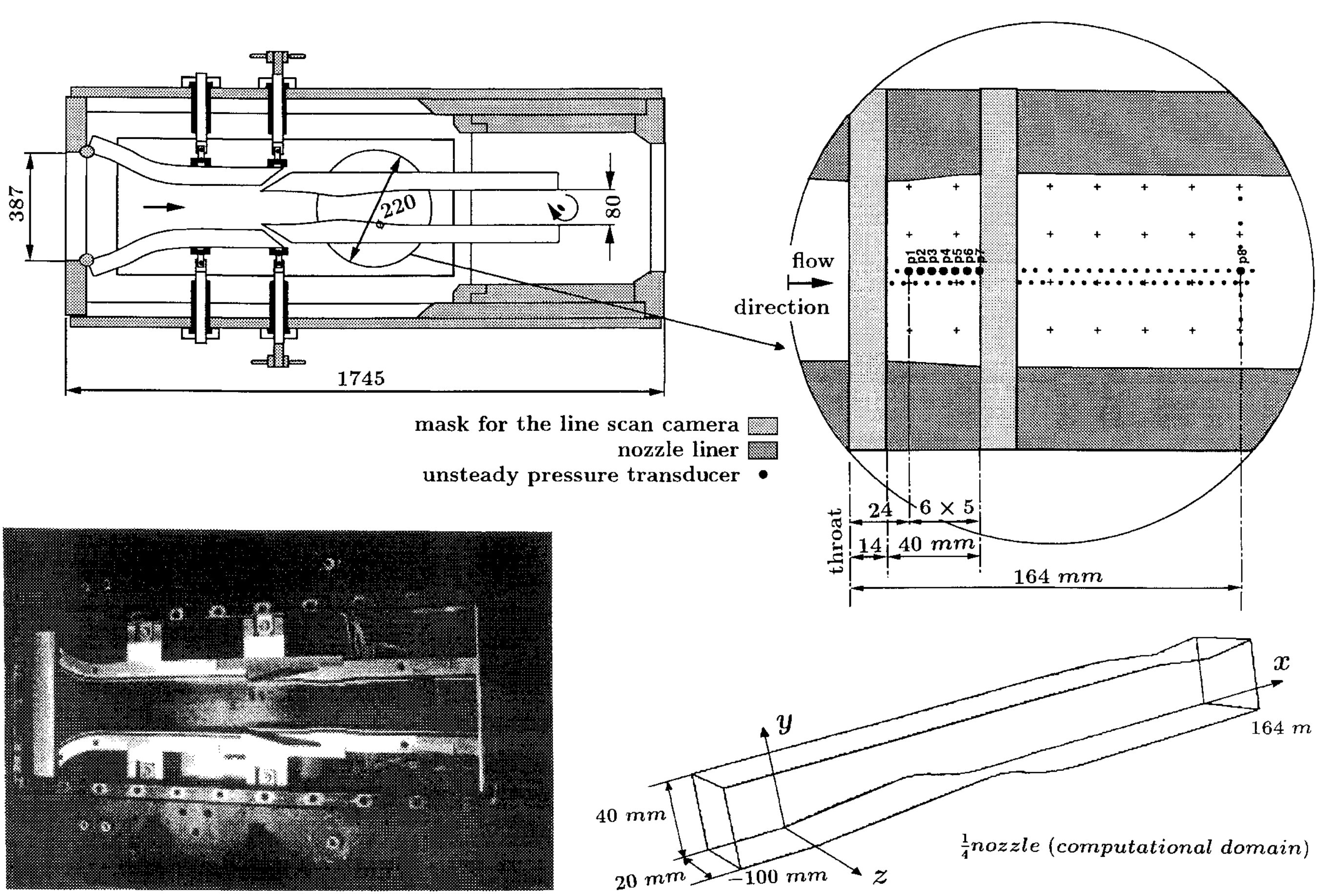

Fig. 1 Experimental setup, computational domain, and system of coordinates.

measurements[23] indicated that the shock wave was practically two dimensional on the y-symmetry plane).

Steady pressure measurements were available for two different static-to-total ($\pi_{S-T} = \bar{p}_2/\check{p}_{t_1}$) nozzle-pressure ratios, corresponding to the nonrotating rod horizontal ($\pi_{S-T} = 0.6360$) or vertical ($\pi_{S-T} = 0.6690$). Steady three-dimensional computations were run for both cases, using a ($121 \times 67 \times 67$) grid, with $y_w^+ \cong z_w^+ \cong 0.5$ (Table 1). The computational grids used in this study consist of planes normal to the x axis, equidistant x wise. The grid is geometrically stretched (with ratio r_y and r_z) in the y- and z-wise directions.[26] At inflow, the experimentally determined conditions were applied [inflow conditions are denoted by $(\cdot)_1$ and outflow conditions by $(\cdot)_2$]:

$$\check{p}_{t_1} = 168600\,\text{Pa}; \qquad \check{T}_{t_1} = 323\,\text{K}; \qquad \check{\delta}_{y_1} = 0.5\,\text{mm}$$
$$\check{\delta}_{z_1} = 5\,\text{mm}; \qquad T_{u_1} = 1.6\%; \qquad l_{T_1} = 0.3\,\text{mm} \tag{6}$$

where $\check{\delta}_{y_1}$ is the boundary-layer thickness at inflow on the nozzle liners, $\check{\delta}_{z_1}$ is the boundary-layer thickness at inflow on the sidewall, $\check{p}_{t_1}$ is the inflow total pressure outside the boundary layers, $\check{T}_{t_1}$ is the inflow total temperature outside the boundary layers, $T_{u_1} = \sqrt{(\frac{2}{3}k_1)}\check{V}_1^{-1}$ is the turbulence intensity at inflow, and $l_{T_1} = k_1^{3/2}\varepsilon_1^{*-1}$ is the turbulence length scale at inflow. The value of $\check{T}_{t_1}$ is an average value, because during the measurements $\check{T}_{t_1}$ varied in the range 313–333 K. The boundary-layer thicknesses at inflow were approximately chosen to represent the thick sidewall boundary layers and the effect of removing the boundary layers on the liners (Fig. 1). The comparison of computed and measured isentropic wall Mach number

$$\check{M}_{is} = \sqrt{[2/(\gamma - 1)]\left[(\check{p}_{t_1}/\bar{p})^{(\gamma-1)/\gamma} - 1\right]} \tag{7}$$

distributions at the y-symmetry-plane on the sidewall (Fig. 2) shows quite satisfactory agreement. The same plot (Fig. 2) includes the two-dimensional result obtained with the three-dimensional code run in pseudo-two-dimensional mode on the same grid ($\pi_{S-T} = 0.6690$). It is evident that three-dimensional effects are important. This is clearly seen in the iso-Machs, at various distances away from the sidewall (Fig. 2), indicating a substantial corner separation. It is impossible to obtain two-dimensional results for the $\pi_{S-T} = 0.6360$ case, because this pressure ratio is lower than the shock-at-exit pressure ratio.

Unsteady Flow Results

Computational Procedure

Unsteady computations were initialized from a converged steady-state flowfield, corresponding to the arithmetic mean π_{S-T} between the two extreme positions of the rod. It was assumed that this arithmetic mean is a good approximation to the time-average unsteady flow ${}^0\pi_{S-T}$ (only dynamic unsteady signals were available in the experiment). The computations were performed for a rod rotation frequency $f = 180$ Hz. The exit of the computational grid coincides with the downstream unsteady pressure probe location ($x = 164$ mm). The computations were started at a negative time ($t = -t_0 \cong -1.775$ ms) corresponding to the nearest to the origin zero-crossing of the experimental signal[24] (Fig. 3). The measured signal contains several harmonics. It is necessary to use the exact measured signal to obtain accurate results.[24]

To reduce computing-time requirements, it was attempted to use coarser grids. Increasing n_w^+ is tempting because the minimum time step is encountered in the cells nearest to the wall, and scales with n_w^{+2} [Eq. (4)]. However, the influence of n_w^+ on the results is known to be significant, especially in three-dimensional flows with corner separation.[18,26] This is illustrated by the comparison of steady-state results using different grids (Table 1) for the mean π_{S-T} (Fig. 4). The grid with $n_w^+ \cong 1.5$ greatly underpredicts the shock-wave strength, and fails to predict the corner separation. However, it was found possible, while retaining $n_w^+ \cong \frac{1}{2}$, to reduce the y- and z-wise grid points, using a $121 \times 57 \times 49$ grid (Table 1), which gives adequate steady-state results (Fig. 4) and contains ~40% fewer points than the 0.52-Mpoints $121 \times 67 \times 67$ grid used for the steady computations.

Table 1 Steady computations summary

π_{S-T}	$N_i(N_x)$	$N_j(N_y)$	$N_k(N_z)$	y_w^+	z_w^+	r_y	r_z	Mpoints[a]	CPU-h[b]
0.6360	121	67	67	0.480	0.500	1.150	1.131	0.52	11
0.6525	101	53	53	1.520	1.536	1.152	1.149	0.27	3
	121	57	49	0.500	0.500	1.182	1.194	0.32	7
	121	67	67	0.500	0.500	1.149	1.131	0.52	11
0.6690	121	67	67	0.500	0.500	1.149	1.131	0.52	11

[a] 1 Mpoint = 1024^2 points. [b] Cray C-98.

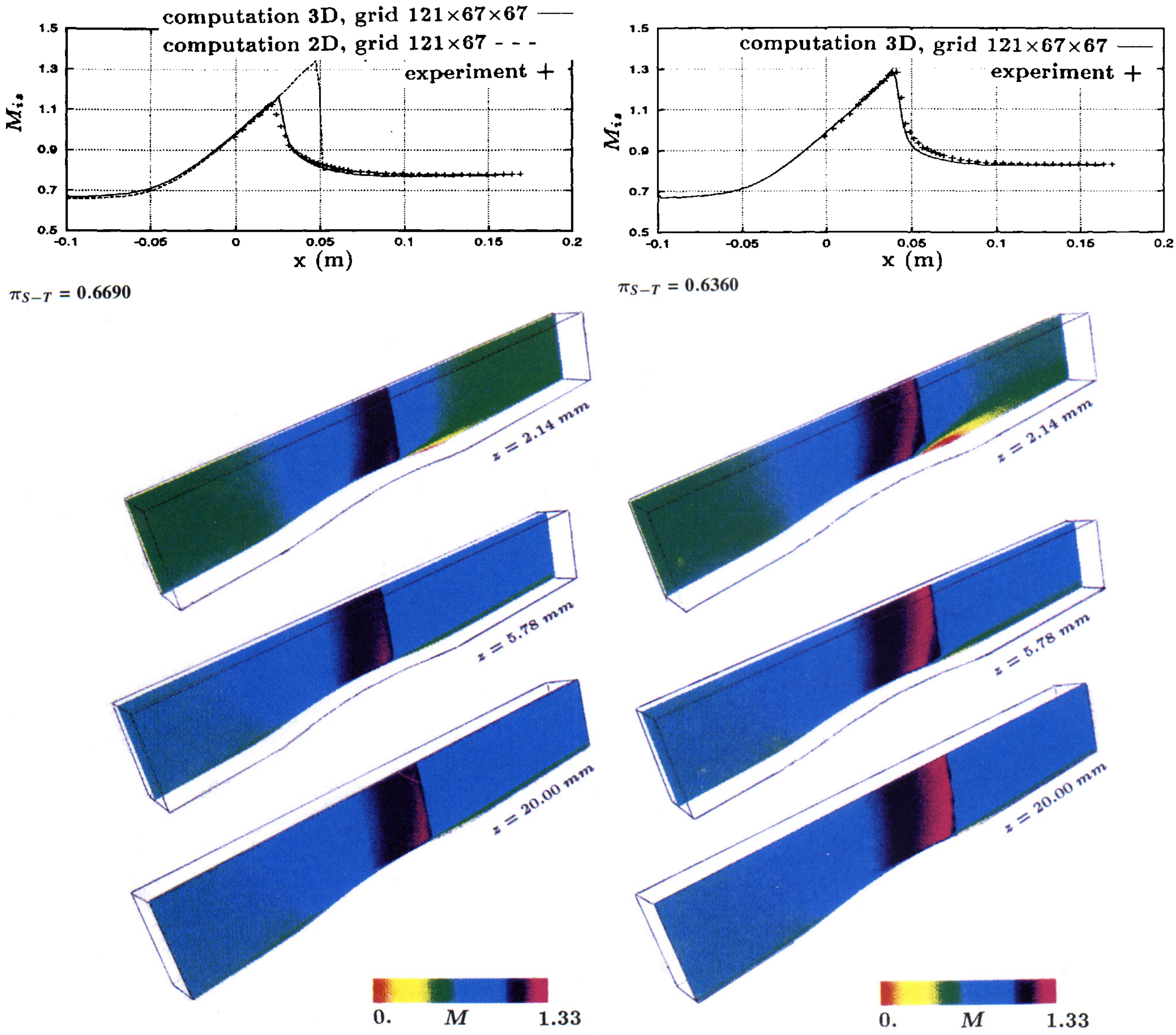

Fig. 2 Comparison of computed and measured M_{is_w} and computed iso-Machs for π_{S-T} = 0.6690, 0.6360.

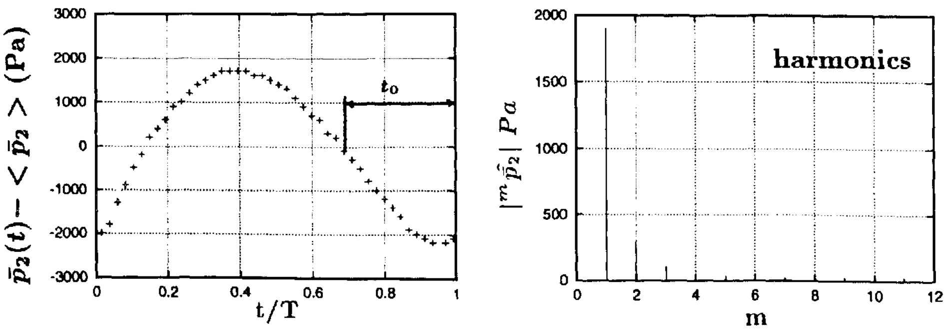

Fig. 3 Measured outflow unsteady pressure signal $\bar{p}_2(t)$.

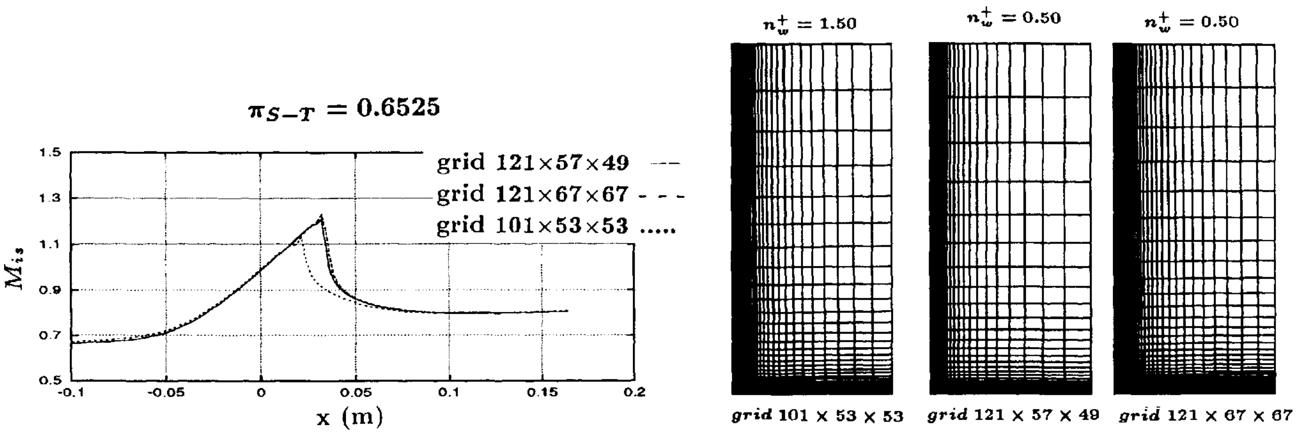

Fig. 4 Grid influence on steady-flow results.

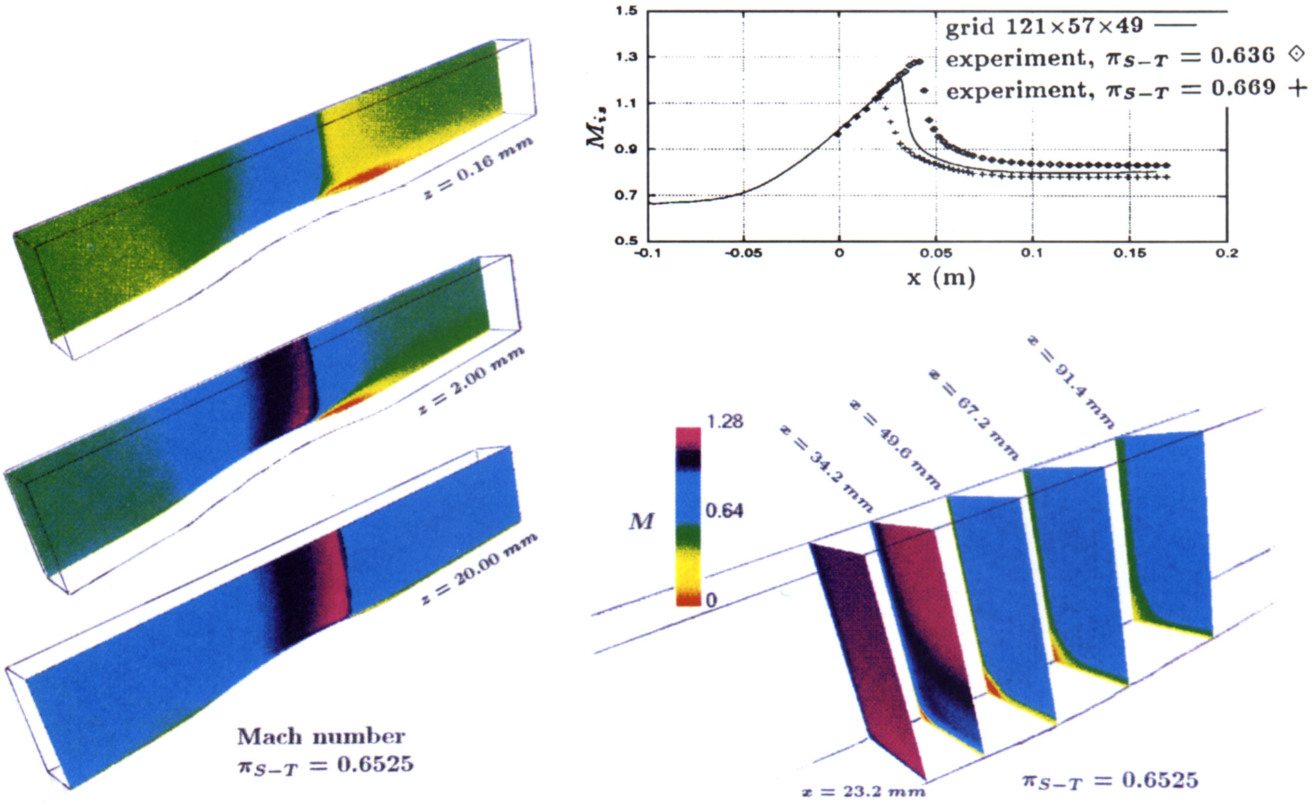

Fig. 5 Computed initial steady-state flowfield (π_{S-T} = 0.6525).

Time integration was performed with a $\Delta t \cong 0.36\,\mu$s, corresponding to $\mathrm{CFL_{max}} \cong 500$. The rather substantial computational times required did not permit a study of $\mathrm{CFL_{max}}$ influence. It was preferred to use this low $\mathrm{CFL_{max}} \cong 500$ rather than risk computational divergence. There are 15,408 instants/period corresponding to ~140 CPU-h/period on a Cray C-98 computer. The fact that $\Delta t \ll T(T = f^{-1} = 5.555\ldots$ ms is the oscillation period) justifies the use of an implicit scheme that is only first-order accurate in time (higher time accuracy presumably will be required at high frequencies).

Comparison of Computations with Experiment

Starting at $t = -t_0 \cong -1.775$ ms from the mean steady-state flowfield (Fig. 5), the computations were continued until $t = 2T$ (corresponding to ~335 CPU-h on a Cray C-98 computer). Unsteady pressures were computed as $\bar{p}(t) - \langle\bar{p}\rangle$:

$$\langle\bar{p}\rangle \equiv {}^0\bar{p} = f\int_T^{2T} \bar{p}(t)\,\mathrm{d}t \tag{8}$$

Comparisons of computed and measured unsteady pressures (Fig. 6) show remarkable agreement between computation and experiment. The pressure signal propagates upstream and induces an oscillation of the shock wave. There is a slight error at the shock wave foot, which can be attributed to the associated error in shock-wave position. An even more interesting comparison is given by the x-wise distributions of the first three harmonics of pressure:

$${}^m\hat{\bar{p}} = \Re({}^m\hat{\bar{p}}) + i\Im({}^m\hat{\bar{p}}) = 2f\int_T^{2T} \bar{p}(t)\exp(-i2\pi m f t)\,\mathrm{d}t \tag{9}$$

The agreement in amplitude distribution is excellent (Fig. 7). The error in the real-part distribution of ${}^1\hat{\bar{p}}$ at the shock-wave foot corresponds to the phase error observed in the time plots. The time plots illustrate the periodic convergence of the computations. The rapidity of periodic convergence (only two periods) also was observed in the two-dimensional Euler computations of Gerolymos and Bréus.[24] The unsteady results agree even better with the experiment than the steady results.

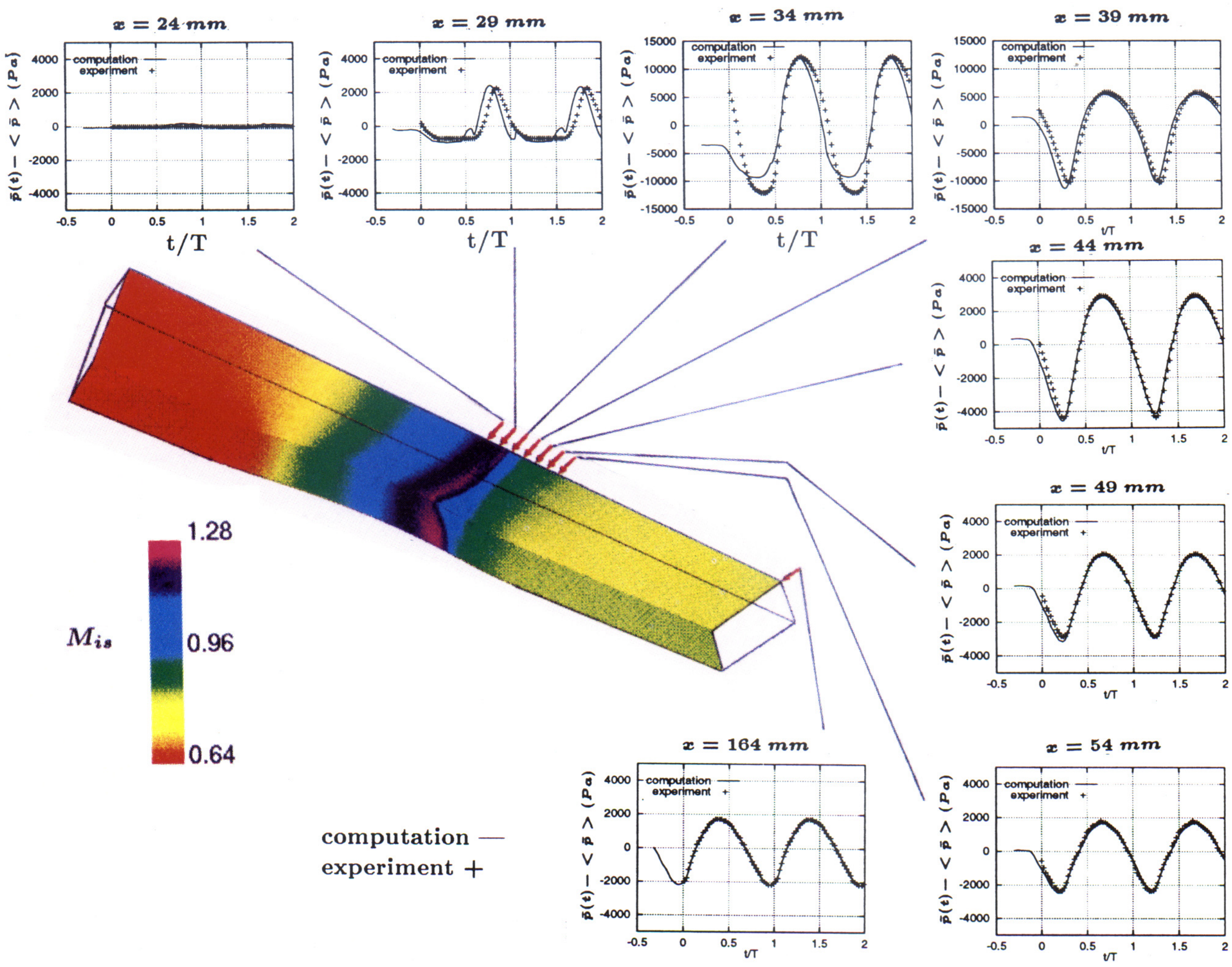

Fig. 6 Comparison of computed and measured unsteady pressures.

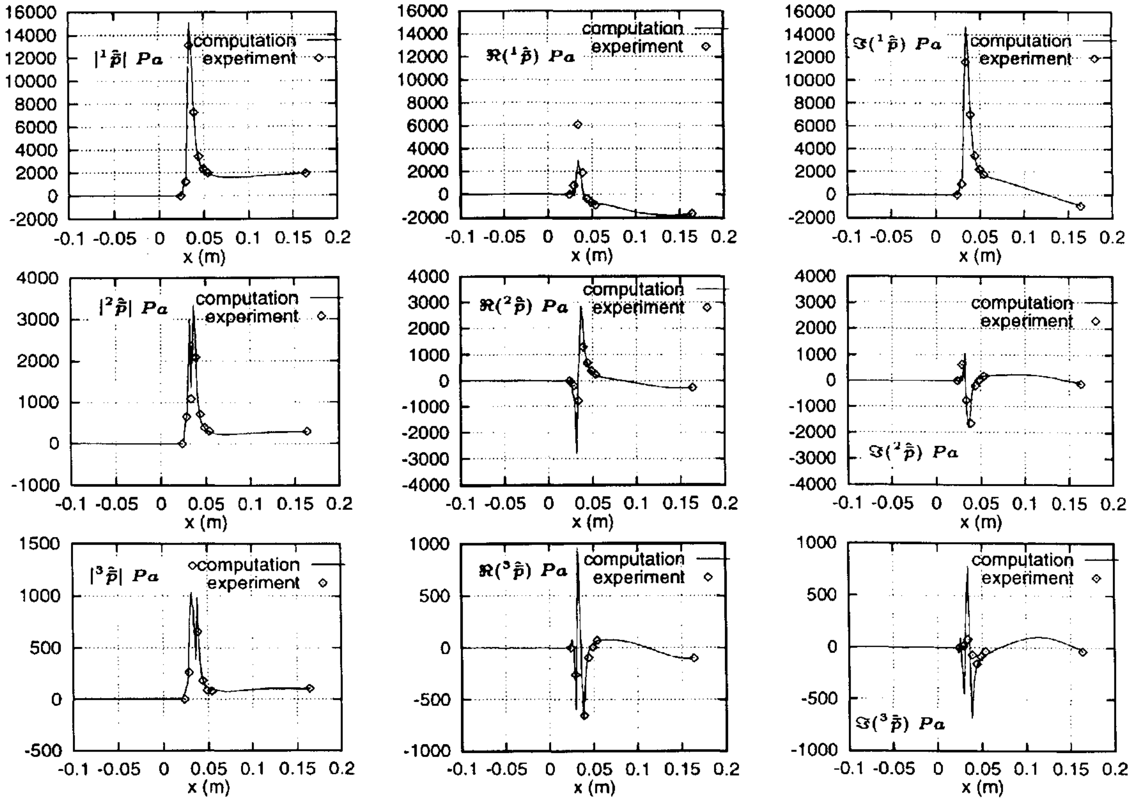

Fig. 7 Comparison of computed and measured pressure-harmonics distributions $^m\hat{\tilde{p}}(x)$ [Eq. (9)].

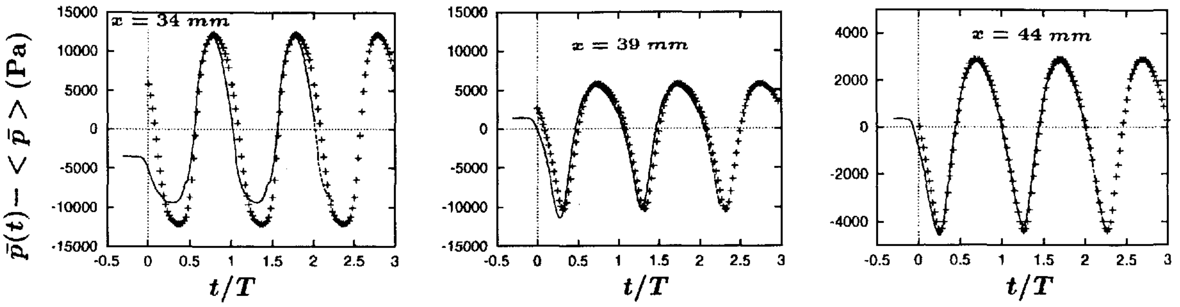

Fig. 8 Influence of Δt on pressure histories: ——, Δt = 0.36 μs, $t < 2T$; - - - -, Δt = 0.18 μs; $t > 2T$; and +, experiment.

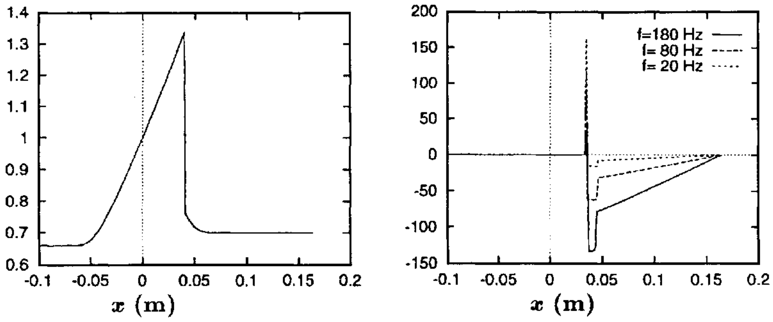

Fig. 9 Influence of frequency on unsteady results using a $1\frac{1}{2}$-dimensional Euler model: steady-state Mach-number and $\angle^1\hat{\bar{p}} - \angle^1\hat{\bar{p}}_2$, deg.

Temporal Accuracy

The numerical scheme used is formally only first-order accurate in time, and approximate factorization of the implicit operator introduces further errors. To confirm the accuracy of the method for the configuration studied, further computations were run, for one-fourth of a cycle, after reducing Δt by one-half ($\Delta t \cong 0.18$ μs corresponding to 30,744 instants/period). Pressure histories at the probes located at $x = 34$, 39, and 44 mm (Fig. 8) demonstrate that results with $\Delta t \cong 0.18$ and 0.36 μs are practically identical.

Reduced Frequency and Unsteady Effects

Although the frequency is rather low, the flow is not quasisteady. This can be demonstrated easily by computing the same configuration at a lower frequency and comparing results. The three-dimensional Navier–Stokes computations being quite time-consuming, it was preferred to use a $1\frac{1}{2}$-dimensional Euler model to illustrate the effect of frequency on unsteady results. We use the same geometry, and the $1\frac{1}{2}$-dimensional Euler equations were solved using the same third-order upwind-biased Van Leer space discretization, but with a second-order-accurate explicit two-stage Runge–Kutta time integration.[24] The outflow perturbation was purely harmonic with an amplitude $|^1\hat{\bar{p}}_2| = 2000$ Pa. Results are presented after the simulation of three cycles. The x-wise distributions of the computed phase angle ($\angle^1\hat{\bar{p}}(x)$–$\angle^1\hat{\bar{p}}_2$) for three different frequencies ($f = 20, 80$, and 180 Hz) show substantial differences between these three frequencies (Fig. 9).

Even for the lowest frequency ($f = 20$ Hz), which is almost 10 times less than the experimental frequency ($f = 180$ Hz), the results are not quasisteady. The frequency and bump chord considered are representative of the first-bending mode of aircraft-engine fans,[12, 13] and the need for unsteady computations should be stressed.

Compressibility Effects on Turbulence

The turbulence closure used is a straightforward extension to compressible flow of the incompressible Launder–Sharma model.[7] Examination of the turbulence Mach number for both steady and unsteady flow shows[27] that $M_T < 0.28$, suggesting that compressibility effects on turbulence are not particularly important for the configuration studied.

Steady and Unsteady Losses

The determination of loss production mechanisms is a problem of major interest in internal flows.[29] For unsteady transonic flows with an oscillating shock wave, Ng and Epstein[30] have suggested an unsteady loss production mechanism by the oscillating shock wave. In their quasisteady model, the nonlinear variation of entropy increase across the shock wave (variation attributable to the modification of the shock-wave strength during the oscillation cycle) produces a difference between the steady entropy production and the time-mean one. This supplementary unsteady loss was rather small. To quantify losses, the mass-flow-weighted x-wise entropy distribution is appropriate[29]:

$$\check{s} = \frac{1}{\dot{m}} \int_0^{B_y} \int_0^{B_z} \bar{\rho}\tilde{u}\check{s}\, \mathrm{d}y\, \mathrm{d}z; \qquad \dot{m} = \int_0^{B_y} \int_0^{B_z} \bar{\rho}\tilde{u}\, \mathrm{d}y\, \mathrm{d}z \tag{10}$$

where $\bar{\rho}$ is the density, $\tilde{u}$ is the x component of velocity, $\check{s}$ is the entropy, $B_y(x)$ is the height of the nozzle, $B_z = 0.04$ m is the width of the nozzle, and $\dot{m}$ is the mass flow ($\dot{m}_{1/4} = 0.263$ kgs is the mass-flow for the one-quarter of the nozzle that was discretized). The entropy $\check{s}$ is computed[31] as a difference from a reference entropy s_{ISA} corresponding to standard conditions ($\check{p}_t = 101{,}325$ Pa, $\check{T}_t =$ 288 K):

$$\check{s} - s_{ISA} = \frac{\gamma}{\gamma - 1} R_g \ln\left(\frac{\check{T}_t}{288}\right) - R_g \ln\left(\frac{\check{p}_t}{101{,}325}\right) \tag{11}$$

The total temperature used did not contain the turbulence kinetic energy ($\check{h}_t = \tilde{h} + \frac{1}{2}\tilde{V}^2 \neq \check{h}_t = \tilde{h} + \frac{1}{2}\tilde{V}^2 + k$) (Ref. 26), and total pressure is computed using the isentropic law[31] [$\check{p}_t = \bar{p}(\check{T}_t/\tilde{T})^{\gamma/(\gamma-1)}$].

Consideration of the steady entropy levels (Fig. 10) indicates the entropy production loci. In the entrance region, entropy is concentrated in the boundary layers, and its value at the wall is ~46 J kg^{-1} K^{-1} + s_{ISA} (the inflow entropy at the nozzle axis is $\check{s}_1 \cong -34$ J kg^{-1} K^{-1} + s_{ISA}). The entropy in the boundary layer increases strongly in the supersonic acceleration region. This increase is easily explained (and quantified) by considering that wall pressure in the region upstream of the shock wave is approximately equal to the static pressure at the boundary-layer edge, and that wall

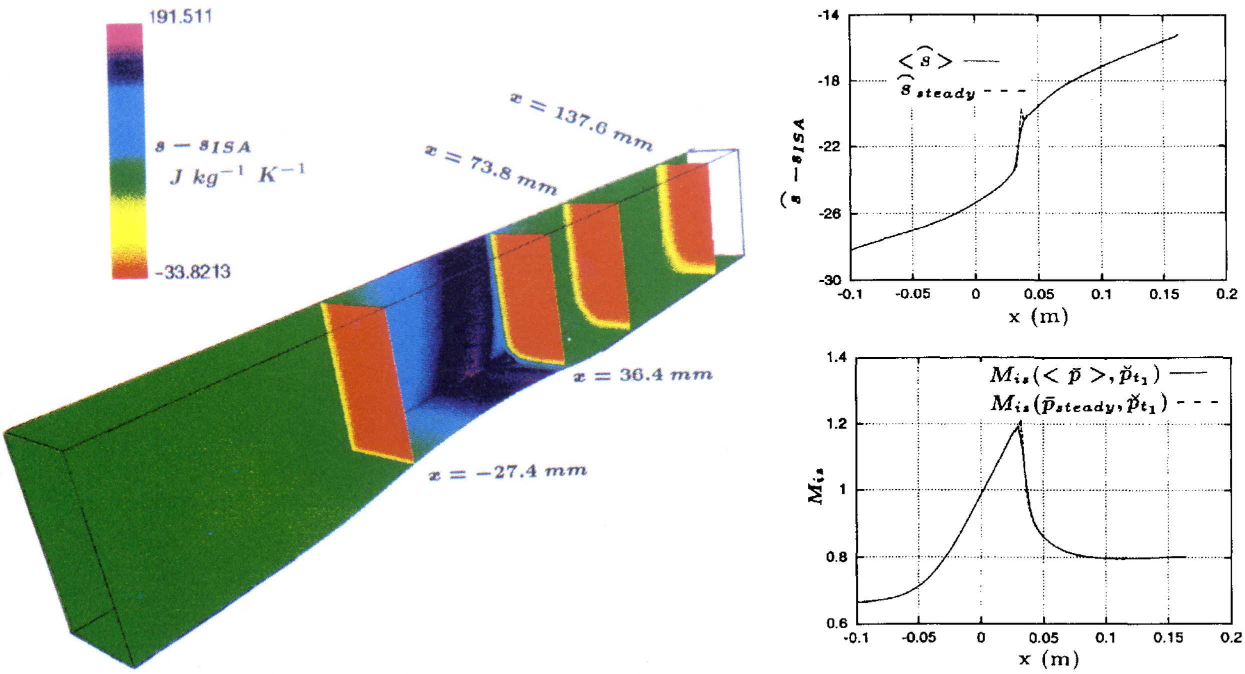

Fig. 10 Steady isoentropy plots and steady and unsteady $\widehat{s}\,(x)$ distributions.

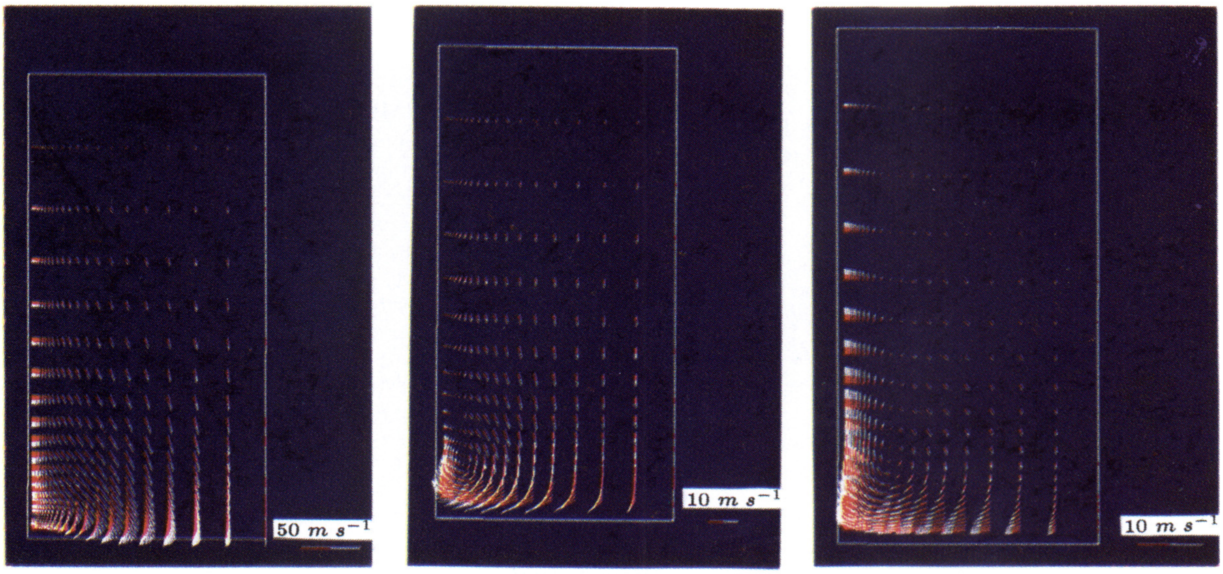

x = 47.4 mm x = 73.8 mm x = 137.6 mm

Fig. 11 Secondary velocity vectors $\tilde{V} - \tilde{u}e_x$ for the steady flow.

temperature is equal to the recovered part of the total temperature at the boundary-layer edge[32]:

$$\breve{p}_{t_w} \equiv \bar{p}_w \cong \bar{p}_e$$

$$\begin{aligned}\breve{T}_{t_w} \equiv \tilde{T}_w &\cong \tilde{T}_e\left(1 + r_f\frac{\gamma - 1}{2}\breve{M}_e^2\right)\\ &= \breve{T}_{t_e}\left\{\frac{1 + r_f[(\gamma - 1)/2]\breve{M}_e^2}{1 + [(\gamma - 1)/2]\breve{M}_e^2}\right\}\\ &\equiv \breve{T}_{t_e}\left\{1 - \frac{(1 - r_f)[(\gamma - 1)/2]\breve{M}_e^2}{1 + [(\gamma - 1)/2]\breve{M}_e^2}\right\}\end{aligned} \tag{12}$$

where $\breve{p}_{t_w}$ is the wall total pressure, $\bar{p}_w$ is the wall pressure, $\breve{T}_{t_w}$ is the wall total temperature, $\tilde{T}_w$ is the wall temperature, $\tilde{T}_e$ is the static temperature at the boundary-layer edge, $\breve{M}_e$ is the Mach-number at the boundary-layer edge, and r_f is the recovery factor[32] ($r_f \cong 0.89$).

Considering that static-pressure decrease at the edge of the boundary layer is quasi-isentropic between the inflow and the supersonic region, that $\breve{T}_{t_e}$ is constant between inflow and outflow, and that $\breve{M}_e \cong 1.2$ at the end of the supersonic region, the wall-entropy increase is

$$\begin{aligned}\breve{s}_w - \breve{s}_{w_1}&\\ &\cong \frac{\gamma}{\gamma - 1}R_g\,\ell n\left\{\frac{1 + r_f[(\gamma - 1)/2]\breve{M}_e^2}{1 + r_f[(\gamma - 1)/2]\breve{M}_1^2}\quad\frac{1 + [(\gamma - 1)/2]\breve{M}_1^2}{1 + [(\gamma - 1)/2]\breve{M}_e^2}\right\}\\ &- \frac{\gamma}{\gamma - 1}R_g\,\ell n\left\{\frac{1 + [(\gamma - 1)/2]\breve{M}_1^2}{1 + [(\gamma - 1)/2]\breve{M}_e^2}\right\} \cong 152\,\mathrm{J\,kg^{-1}\,K^{-1}}\end{aligned} \tag{13}$$

where $\breve{M}_1 \cong 0.67$ is the Mach number at inflow and $\breve{s}_{w_1} \cong +46\,\mathrm{J\,kg^{-1}\,K^{-1}} + s_{ISA}$ is the wall entropy at inflow. This increased entropy is still contained in the boundary layers. It induces nonetheless an increasing slope in the entropy distribution before the shock

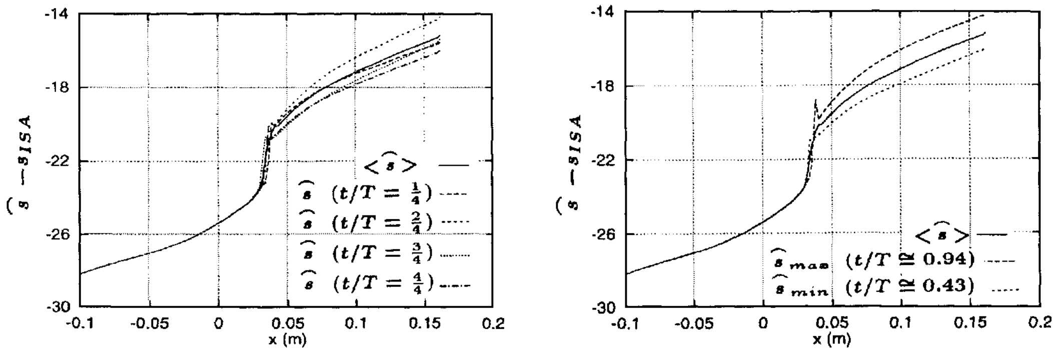

Fig. 12 Unsteady variation of $\widehat{s}\ (x, t)$.

wave. The interaction of the shock wave with the corner boundary layer induces a separated zone of high entropy. The high-entropy region diffuses away from the wall downstream. This is because of the secondary flows that appear after the shock wave–boundary layer interaction (Fig. 11). The plot of secondary velocity vectors $(\tilde{V} - \tilde{u}e_x)$ shows clearly the secondary vortex that moves progressively away from the wall and transports the high-entropy fluid toward the center. The entropy at the nozzle axis increases continuously downstream of the shock wave because of this mixing effect.

For the flow studied here, there are virtually no unsteady effects on time-mean loss-production. The steady flow entropy distribution $\widetilde{s}_{\text{steady}}$ and the time-mean value

$$\langle \widehat{s} \rangle \equiv {}^{0}\widehat{s} = f \int_{T}^{2T} \widehat{s}\,(x, t)\,\mathrm{d}t \tag{14}$$

are practically identical except in the immediate neighborhood of the shock wave, where shock motion smears the entropy jump across the shock wave over a greater distance than for steady flow (Fig. 10). This smearing is also observed in the steady and time-mean isentropic-wall Mach-number distributions (Fig. 10).

The fact that the steady and time-averaged losses are quasi-identical (in fact, the time-averaged losses are slightly less) does not mean that losses do not vary with time. On the contrary, the mass-flow-weighted outflow entropy $\widetilde{s}_2$ varies by $\pm 1\ \mathrm{J\,kg^{-1}\,K^{-1}}$ during the oscillation cycle (Fig. 12). This variation apparently does not induce any nonlinear unsteady losses, a finding that suggests that the coupled shock wave–corner separation loss-generation mechanism is more complex than the simple oscillating shock model of Ng and Epstein.[30] Note, however, that in the particular case studied, viscous losses are important because of the small width of the nozzle.

Conclusions

The unsteady flow in a three-dimensional nozzle with thick sidewall boundary layers, caused by backpressure fluctuation produced experimentally by a rotating rod of elliptical cross section, was studied using a three-dimensional Navier–Stokes solver with near-wall k–ε closure. A $121 \times 57 \times 49$ grid was used to discretize one-fourth of the nozzle (using a double-symmetry condition). This grid was chosen such that the first grid point is at $n_w^+ = 0.5$, for both the lower wall and the sidewall. A steady-flow grid-influence study showed that this grid gives grid-independent results. The three-dimensional effect is produced by the shock wave–boundary layer interaction at the corners of the nozzle, where an important three-dimensional recirculating zone appears. At inflow, a 0.5-mm turbulent-boundary-layer profile was imposed on the lower wall, and a 5-mm turbulent-boundary-layer profile was imposed on the sidewall at the inflow boundary. This corresponds to the experimental setup, where there was no boundary-layer bleed on the sidewalls. The unsteady computations were run with a 0.36-μs time step ($\text{CFL}_{\max} \cong 500$), for a backpressure fluctuation frequency of 180 Hz. To simulate one period, 15,408 iterations are necessary, corresponding to $\sim$140 CPU-h on a Cray C-98 computer. Periodic convergence of the unsteady results was obtained after the simulation of two cycles (+ an initial one-third of a cycle) corresponding to $\sim$335 CPU-h. The computational time required is important because of the rather low frequency. The computed and measured results compare remarkably well.

The question is naturally raised: Why is the agreement of unsteady computation with experiment so good, when a standard turbulence model with well-known drawbacks was used? The computations reported were completely predictive. The measured steady and unsteady outflow pressure was applied as boundary condition in the computations. No adjustment whatsoever was made, and the standard model constants were used (the authors firmly believe that tampering with model constants is an inadmissible practice). The answer to this question is twofold. On the one hand, the steady-flow prediction is, in this case, quite satisfactory, because of the rather low M_{shock} ($\sim$1.2–1.3) and of the strongly three-dimensional nature of the flow (three-dimensional flows are easier to predict than two-dimensional flows, even if computing-time requirements are greater). On the other hand, unsteady predictions are invariably better than steady predictions for driven flows such as those encountered in flutter and forced-response analyses. It is believed, therefore, that improvement of unsteady predictions in such cases hinges upon bettering the prediction of the underlying steady flow.

The grid-influence study conducted for this configuration agrees with previous results that n_w^+ is the most important grid-quality parameter. Even if using $n_w^+ = 0.5$–0.75 is time-consuming for unsteady computations, it is indispensible to do so for the quality of steady and unsteady results.

It is clear, despite the satisfactory results obtained in this study, that experimental validation was only partial. Even if unsteady pressures were exceptionally well predicted (and unsteady pressures are very important for practical applications), there was no way of assessing the prediction of several difficult flow characteristics, such as velocity profiles and wall shear stresses. There is a need for experimental data that would permit such validation in realistic three-dimensional configurations. It is also important to develop a validation database for higher frequencies, for which spectral interaction between the driving unsteady phenomenon and turbulence is possible. In the present case, $f^+ \cong 2 \times 10^{-5}$ (based on inflow boundary-layer parameters and $f = 180$ Hz), which is well away from the region where spectral interaction is possible.

From a numerical and modeling point of view, the necessary improvements are obvious: improve turbulence modeling, for improved steady-flow prediction, using near-wall Reynolds stress closure; extend the implicit scheme to second-order time accuracy (using three-point backward time-discretization with Newton subiterations) for better prediction at high frequencies.

Acknowledgments

The computations presented in this work were run at the Institut pour le Développement des Ressources en Informatique Scientifique, where computer ressources were made available by the Comité Scientifique. Authors are listed alphabetically by institution.

References

[1] Ekaterinaris, J. A., and Menter, F. R., "Computation of Oscillating Airfoil Flows with One- and Two-Equation Turbulence Models," *AIAA Journal*, Vol. 32, No. 12, 1994, pp. 2359–2365.

[2] Rizzetta, D. P., and Visbal, M. R., "Comparative Numerical Study of Two Turbulence Models for Airfoil Static and Dynamic Stall," *AIAA Journal*, Vol. 31, No. 4, 1993, pp. 784–786.

[3] Jin, G., and Braza, M., "Two-Equation Turbulence Model for Unsteady Separated Flows Around Airfoils," *AIAA Journal*, Vol. 32, No. 11, 1994, pp. 2316–2320.

[4] Shih, S. H., Hamed, A., and Yeuan, J. J., "Unsteady Supersonic Cavity Flow Simulations Using Coupled k–ε and Navier–Stokes Equations," *AIAA Journal*, Vol. 32, No. 10, 1994, pp. 2015–2021.

[5] Rizzetta, D. P., "Numerical Simulation of Supersonic Flow over a 3-D Cavity," *AIAA Journal*, Vol. 26, 1988, pp. 799–807.

[6] Fan, S., Lakshminarayana, B., and Barnett, M., "Low-Reynolds-Number k–ε Model for Unsteady Turbulent Boundary-Layer Flows," *AIAA Journal*, Vol. 31, No. 10, 1993, pp. 1777–1784.

[7] Launder, B. E., and Sharma, B. I., "Application of the Energy Dissipation Model of Turbulence to the Calculation of Flows Near a Spinning Disk," *Letters in Heat Mass Transfer*, Vol. 1, 1974, pp. 131–138.

[8] Guruswamy, G. P., "Integrated Approach for Active Coupling of Structures and Fluids," *AIAA Journal*, Vol. 27, 1989, pp. 788–793.

[9] Batina, J. T., "Unsteady Euler Airfoil Simulations Using Unstructured Dynamic Meshes," *AIAA Journal*, Vol. 28, 1990, pp. 1381–1388.

[10] Batina, J. T., "Unsteady Euler Algorithm with Unstructured Dynamic Mesh for Complex-Aircraft Aerodynamic Analysis," *AIAA Journal*, Vol. 29, 1991, pp. 327–333.

[11] Obahashi, S., Guruswamy, G. P., and Goorjian, P. M., "Streamwise Upwind Algorithm for Computing Unsteady Transonic Flows Past Oscillating Wings," *AIAA Journal*, Vol. 29, 1991, pp. 1668–1677.

[12] Gerolymos, G. A., "Advances in the Numerical Integration of the 3-D Euler Equations in Vibrating Cascades," *Journal of Turbomachinery*, Vol. 115, 1993, pp. 781–790.

[13] Gerolymos, G. A., "Coupled 3-D Aeroelastic Stability Analysis of Bladed Disks," *Journal of Turbomachinery*, Vol. 115, 1993, pp. 791–800.

[14] Tardu, S. F., and Binder, G., "Wall Shear Stress Modulation in Unsteady Turbulent Channel Flow with High Imposed Frequencies," *Physics of Fluids*, Vol. 5, 1993, pp. 2028–2037.

[15] Hankey, W. L., and Calarese, W., "Reynolds Stresses for Unsteady Turbulent Flows," *AIAA Journal*, Vol. 21, 1983, pp. 1210, 1211.

[16] Lakshminarayana, B., "Turbulence Modeling for Complex Shear Flows," *AIAA Journal*, Vol. 24, 1986, pp. 1900–1917.

[17] Gerolymos, G. A., "Implicit Multiple-Grid Computation of the Compressible Navier–Stokes Equations Using k–ε Turbulence Closure," *AIAA Journal*, Vol. 28, 1990, pp. 1707–1717.

[18] Rizzetta, D. P., "Numerical Simulation of Slot-Injection into a Turbulent Supersonic Stream," *AIAA Journal*, Vol. 30, 1992, pp. 2434–2439.

[19] Rizzetta, D. P., "Numerical Simulation of Turbulent Cylinder Juncture Flowfields," *AIAA Journal*, Vol. 32, No. 6, 1994, pp. 1113–1119.

[20] Liang, S. M., Tsai, C. J., and Ho, C. K., "Numerical Investigation of Unsteady Transonic Nozzle Flows," *AIAA Journal*, Vol. 30, 1992, pp. 566–568.

[21] Liang, S. M., and Tsai, C. J., "Shock Oscillation in 2-D Inviscid Unsteady Channel Flow," *AIAA Journal*, Vol. 31, 1993, pp. 200–203.

[22] Li, C. C., Messiter, A. F., and Van Leer, B., "Unsteady Transonic Cascade Flow with In-Passage Shock-Wave," *AIAA Journal*, Vol. 28, 1990, pp. 1135–1138.

[23] Ott, P., Bölcs, A., and Fransson, T. H., "Experimental and Numerical Study of the Time-Dependent Pressure Response of a Shock-Wave Oscillating in a Nozzle," *Journal of Turbomachinery*, Vol. 117, 1995, pp. 106–114.

[24] Gerolymos, G. A., and Bréus, J. P., "Computation of Unsteady Nozzle Flow due to Fluctuating Back-Pressure Using Euler Equations," *Recherche Aérospatiale* (submitted for publication); ASME Paper 94-GT-91.

[25] Liou, M. S., and Coakley, T. J., "Numerical Simulations of Unsteady Transonic Flow in Diffusers," *AIAA Journal*, Vol. 22, 1984, pp. 1139–1145.

[26] Gerolymos, G. A., and Vallet, I., "Implicit Computation of Three-Dimensional Compressible Navier–Stokes Equations Using k–ε Closure," *AIAA Journal*, Vol. 34, No. 7, 1996, pp. 1321–1330.

[27] Vallet, I., "Aérodynamique Numérique 3-D Instationnaire avec Fermeture Bas Reynolds au Second Ordre," Doctorat, Univ. Pierre-et-Marie-Curie, Paris, 1995.

[28] MacCormack, R. W., "A Numerical Method for Solving the Equations of Compressible Viscous Flow," *AIAA Journal*, Vol. 20, 1982, pp. 1275–1281.

[29] Denton, J. D., "Loss Mechanisms in Turbomachines," *Journal of Turbomachinery*, Vol. 115, 1993, pp. 621–656.

[30] Ng, W. F., and Epstein, A. H., "Unsteady Losses in Transonic Compressors," *Journal of Engineering for Gas Turbines and Power*, Vol. 107, 1985, pp. 345–353.

[31] Liepmann, H. W., and Roshko, A., *Elements of Gasdynamics*, Wiley, New York, 1957, p. 20.

[32] Van Driest, E. R., "Turbulent Boundary-Layer in Compressible Fluids," *Journal of Aerospace Sciences*, Vol. 18, 1951; pp. 145–160, 216.

Color reproduction courtesy of Laboratoire d'Energétique, Université Pierre-et-Marie-Curie